Electric Supplementary Information for

High-Density Cathode Structure of Independently Acting Prussian-Blue-Analog Nanoparticles: A High-Power Zn–Na-Ion Battery Discharging ~200 mA cm^{-2} at 1000 C

Yuta Asahina, Ryo Terashima, Manabu Ishizaki*, Hideo Ando, Jun Matsui, Hirofumi Yoshikawa, and Masato Kurihara*

**Theoretical calculations of the interaction between $[Fe^{II}(CN)_6]^{4-}$ and a single-walled carbon nanotube (SWNT) model**

Focusing on the contact area between an MHCF NP and SWNT, we considered a surface modification regent of $[Fe^{II}(CN)_6]^{4-}$ (Fig. A1a), aromatic carbon-ring belt (Fig. A1b) and their cluster (dimer). The carbon-ring belt is designed to model an armchair SWNT (12,12) whose diameter is consistent with the average diameter (1.6 nm) of experimentally used SWNTs. In the model, designated as SWNT (12,12), three rings are arranged along the tube direction, and all dangling bonds at the edges are compensated by H atoms (Fig. A1b). We considered the closed-shell electronic configuration not only for SWNT (12,12) but for $[Fe^{II}(CN)_6]^{4-}$ and the cluster, in which the Fe^{II} center was in a singlet spin state due to a strong ligand field of the C-bonded C≡N. All geometries were fully optimized using the Kohn–Sham density functional theory (DFT) along with B3LYP functional.[1-3] The LanL2DZ effective core potential with associated basis set[4] and the 6-31G(d) basis set[5-7] were employed for Fe and the other atoms, respectively. The effects of the dispersion interaction and hydration were incorporated using Grimme's D3 correction with Becke–Johnson (BJ) damping[8] and the conventional polarizable continuum model (PCM),[9] respectively. All calculations were performed with Gaussian 16.[10]

Fig. A1 shows equilibrium geometries of $[Fe^{II}(CN)_6]^{4-}$, SWNT (12,12) and the cluster. We obtained two geometries for the cluster: a three-leg structure (Fig. A1c) and a one-leg structure (Fig. A1d). Three N atoms of $[Fe^{II}(CN)_6]^{4-}$ point toward the tube's sidewall in the three-leg structure, whereas only one N atom points toward the sidewall in the one-leg structure. Relative to a noninteracting reference system of $[Fe^{II}(CN)_6]^{4-}$ and SWNT (12,12) at infinite separation (Fig. A1a,b), the three-leg structure is 4.7-kcal/mol lower in potential energy; in other words, the binding energy is 4.7 kcal/mol. The average distance between an N atom that points to the sidewall and its nearby C atom on the sidewall is 3.57 Å. The long distance indicates that $[Fe^{II}(CN)_6]^{4-}$ and SWNT (12,12) noncovalently interact with each other in the three-leg structure. When fixing the optimized geometries and disabling Grimme's dispersion correction, we found that the interaction becomes repulsive; that is, the potential energy of the three-leg structure is 3.7 kcal/mol higher than that of the noninteracting reference system. This result highlights the importance of the dispersion interaction. Besides, it turns out that π-electron polarization of SWNT (12,12) occurs (Fig. A2). The approach of $[Fe^{II}(CN)_6]^{4-}$ to SWNT (12,12) causes the electron density decrease on the exterior of the sidewall (i.e. a planar purple isosurface in Fig. A2a), particularly near the electronegative N atoms (Fig. A2b). Meanwhile, the approach causes an electron density increase around C atoms far from $[Fe^{II}(CN)_6]^{4-}$ (i.e. orange isosurfaces in Fig. A2a). This electronic polarization would induce an electric dipole moment along a transverse direction of the sidewall and, thus, an electrostatic attraction between SWNT (12,12) and the nearby three N atoms. We note that, although purple isosurfaces appear around the three N atoms (Fig. A2), the N atoms are electronegative regardless of the distance between $[Fe^{II}(CN)_6]^{4-}$ and SWNT (12,12). Our theoretical results suggest that the dispersion interaction and the induced electrostatic attraction weakly bind SWNTs with the surface modification regents of $[Fe^{II}(CN)_6]^{4-}$ and/or the dangling C≡N groups of MHCF NPs.

The potential energy of the one-leg structure (Fig. A1d) is 21.1 kcal/mol higher than that of the

noninteracting reference system. Unlike the three-leg structure (Fig. A1c), the one-leg structure forms a covalent bond between an N atom of $[Fe^{II}(CN)_6]^{4-}$ and a C atom of SWNT (12,12) with a bond length of 1.49 Å; indeed, out-of-plane structural distortion occurs at the C atom to form an sp^3-type structure (Fig. A1d), and the Wiberg's bond order,[11] defined in terms of the natural atomic orbital basis, is 0.83 for the relevant N-C bond. The one-leg structure is nothing but a local-energy-minimum geometry. Nevertheless, the covalent bonding between SWNTs and surface modification regents of $[Fe^{II}(CN)_6]^{4-}$ may be formed if the hydration effect is weakened by some possible factors we ignored. For example, the constituent atoms of an MHCF NP can exclude water molecules from the vicinity of a surface $[Fe^{II}(CN)_6]^{4-}$ regent, thereby weakening the hydration effect. Supposing an extreme case of no hydration effect, the binding energy for the one-leg structure, including the contribution of the N-C covalent bond, is 233.5 kcal/mol.
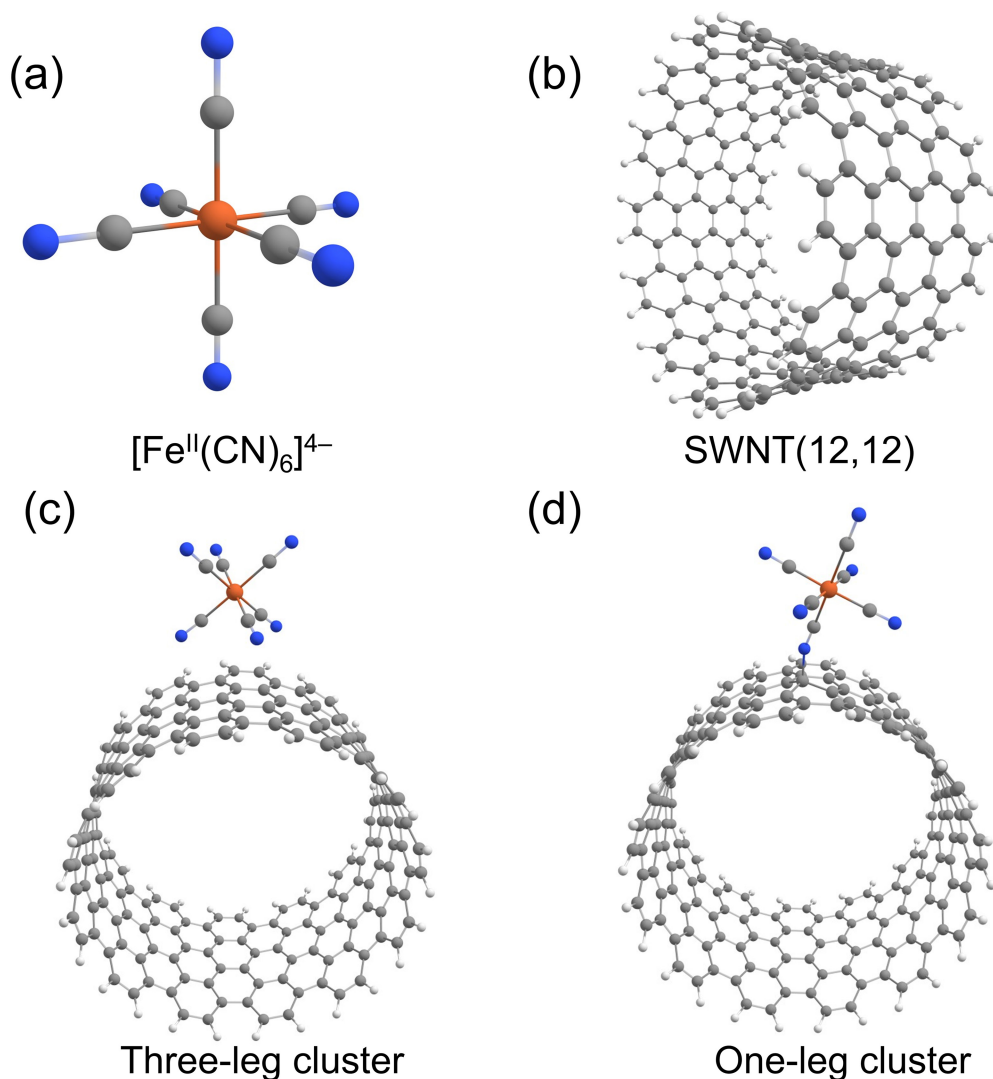
Fig. A1. DFT-optimized geometries of (a) $[Fe^{II}(CN)_6]^{4-}$, (b) SWNT (12,12), (c) three-leg structure, and (d) one-leg structure of the cluster. The Fe, C, N and H atoms are indicated by orange, gray, blue and white balls, respectively.

| | (a) | (b) |
| Side view | | Top view |
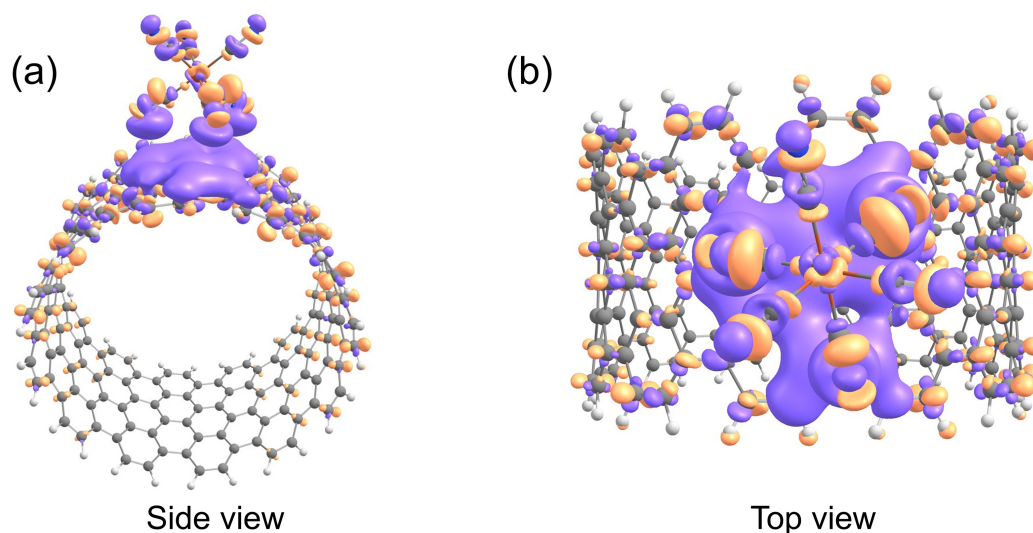
Fig. A2. Differential electron density of the three-leg cluster of (a) side view and (b) top view. To visualize the electron density change due to the approach of $[Fe^{II}(CN)_6]^{4-}$ to SWNT (12,12), the electron density of the noninteracting monomers was subtracted from that of the cluster. The density of the noninteracting monomers was defined by the simple addition of the densities of $[Fe^{II}(CN)_6]^{4-}$ and SWNT (12,12), which were isolated from each other. The isosurface contour values are $+10^{-4}$ e bohr^{-3} (orange isosurfaces) and -10^{-4} e bohr^{-3} (purple isosurfaces).

References

1 A. D. Becke, *J. Chem. Phys.,* 1993, **98**, 5648–5652.

2 C. Lee, W. Yang and R. G. Parr, *Phys. Rev. B,* 1988, **37**, 785–789.

3 B. Miehlich, A. Savin and H. Stoll, H. Preuss, *Chem. Phys. Lett.,* 1989, **157**, 200–206.

4 P. J. Hay and W. R. Wadt, *J. Chem. Phys.,* 1985, **82**, 299–310.

5 R. Ditchfield, W. J. Hehre and J. A. Pople, *J. Chem. Phys.,* 1971, **54**, 724–728.

6 P. C. Hariharan and J. A. Pople, *Theor. Chim. Acta,* 1973, **28**, 213–222.

7 W. J. Hehre, R. Ditchfield and J. A. Pople, *J. Chem. Phys.,* 1972, **56**, 2257–2261.

8 S. Grimme, S. Ehrlich and L. Goerigk, *J. Comput. Chem.,* 2011, **32**, 1456–1465.

9 J. Tomasi, B. Mennucci and R. Cammi, *Chem. Rev.,* 2005, **105**, 2999–3094.

10 Gaussian 16, Revision A.03, M. J. Frisch, G. W. Trucks, H. B. Schlegel, G. E. Scuseria, M. A. Robb, J. R. Cheeseman, G. Scalmani, V. Barone, G. A. Petersson, H. Nakatsuji, X. Li, M. Caricato, A. V. Marenich, J. Bloino, B. G. Janesko, R. Gomperts, B. Mennucci, H. P. Hratchian, J. V. Ortiz, A. F. Izmaylov, J. L. Sonnenberg, D. Williams-Young, F. Ding, F. Lipparini, F. Egidi, J. Goings, B. Peng, A. Petrone, T. Henderson, D. Ranasinghe, V. G. Zakrzewski, J. Gao, N. Rega, G. Zheng, W. Liang, M. Hada, M. Ehara, K. Toyota, R. Fukuda, J. Hasegawa, M. Ishida, T. Nakajima, Y. Honda, O. Kitao, H. Nakai, T. Vreven, K. Throssell, J. A. Montgomery, Jr., J. E. Peralta, F. Ogliaro, M. J. Bearpark, J. J. Heyd, E. N. Brothers, K. N. Kudin, V. N. Staroverov, T. A. Keith, R. Kobayashi, J. Normand, K. Raghavachari, A. P. Rendell, J. C. Burant, S. S. Iyengar, J. Tomasi, M. Cossi, J. M. Millam, M. Klene, C. Adamo, R. Cammi, J. W. Ochterski, R. L. Martin, K. Morokuma, O. Farkas, J. B. Foresman and D. J. Fox, Gaussian, Inc., Wallingford CT, 2016.

11 K. B. Wiberg, *Tetrahedron,* 1968, **24**, 1083–1096.

Ragone plots

Representative high-performance non-aqueous and neutral aqueous ZnIBs and Zn-KIBs[1–5] and non-aqueous high-operating voltage K/NaIBs using MHCFs [6–9] are listed. To approach the orders of magnitude higher range (undeveloped range) in Ragone plots (pathway 2 of Fig. 6b), the energy densities of supercapacitors have been improved by combining redox reactions and/or by using activated porous carbon.[10–13] The energy densities considerably decrease at ultrahigh C rates. In contrast, the RSW cathodes suppress such energy-density loss to occupy the undeveloped range. The energy- and power-density values were extracted from the data[1,2,5,10–13] or estimated from the charge/discharge profiles based on Fig. S9d,e.[3,4,6–9]
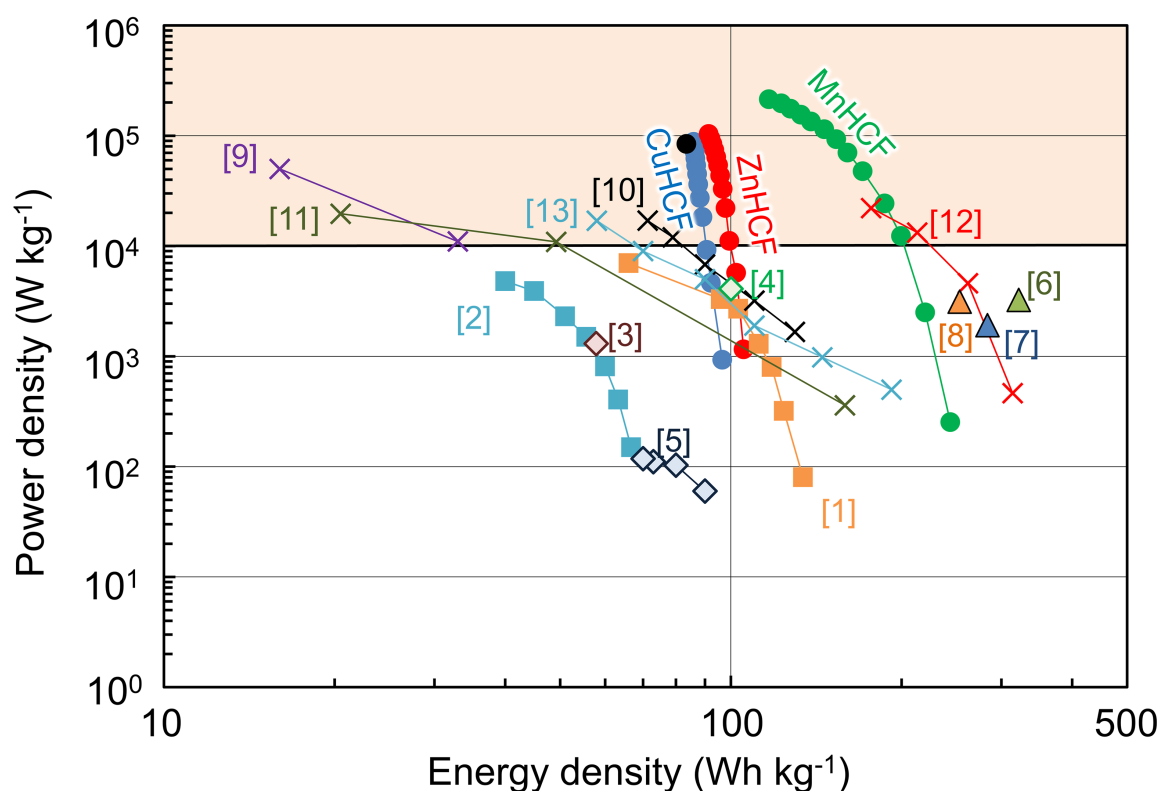
References

Zn–KIBs

1 Q. Li, K. Ma, C. Hong, Z. Yang, C. Qi, G. Yang and C. Wang, *Energy Storage Mater.,* 2021, **42**, 715–722.

2 M. Huang, J. Meng, Z. Huang, X. Wang and L. Mai, *J. Mater. Chem. A,* 2020, **8**, 6631–6637.

ZnIBs

3 F. Ming, Y. Zhu, G. Huang, A.-H. Emwas, H. Liang, Y. Cui and H. N. Alshareef, *J. Am. Chem. Soc.,* 2022, **144**, 7160–7170.

4 Y. Zhang, Y. Wang, L. Lu, C. Sun and D. Y. W. Yu, *J. Power Sources,* 2021, **484**, 229263.

5 Q. Li, K. Ma, G. Yang and C. Wang, *Energy Storage Mater.,* 2020, **29**, 246–253.

High-operating voltage Na/KIBs

6 J. Peng, Y. Gao, H. Zhang, Z. Liu, W. Zhang, L. Li, Y. Qiao, W. Yang, J. Wang, S. Dou and S. Chou, *Angew. Chem. Int.*

Ed., 2022, **61**, e202205867.

7 L. Deng, J. Qu, X. Niu, J. Liu, J. Zhang, Y. Hong, M. Feng, J. Wang, M. Hu, L. Zeng, Q. Zhang, L. Guo and Y. Zhu, *Nat. Commun.,* 2021, **12**, 2167.

8 P. Ge, S. Li, H. Shuai, W. Xu, Y. Tian, L. Yang, G. Zou, H. Hou and X. Ji, *Adv. Mater.,* 2019, **31**, 1806092.

High energy-density supercapacitors/pseudocapacitors

9 X. Fan, K. Huang, L. Chen, H. You, M. Yao, H. Jiang, L. Zhang, C. Lian, X. Gao and C. Li, *Angew. Chem. Int. Ed.,* 2023, **62**, e202215342.

10 J. Zhang, J. Luo, Z. Guo, Z. Liu, C. Duan, S. Dou, Q. Yuan, P. Liu, K. Ji, C. Zeng, J. Xu, W.-D. Liu, Y. Chen and W. Hu, *Adv. Energy Mater.,* 2023, **13**, 2203061.

11 C. Xu, J. Mu, T. Zhou, S. Tian, P. Gao, G. Yin, J. Zhou and F. Li, *Adv. Funct. Mater.,* 2022, **32**, 2206501.

12 J. Zhang, J. Zhang, H. Wang, V. W.-h. Lau, G.-H. Lee, K. Zhang, M. Park and Y.-M. Kang, *ACS Energy Lett.,* 2022, **7**, 4472–4482.

13 L. Yang, L. Song, Y. Feng, M. Cao, P. Zhang, X.-F. Zhang and J. Yao, *J. Mater. Chem. A,* 2020, **8**, 12314–12318.

Table S1. Current densities of Zn–NaIBs using RSW model cathodes depending on loading amounts of ZnHCF NPs

Loading amounts (mg cm^{-2})	Current densities (mA cm^{-2})/C rates		#Electrolyte conditions
	Charge	Discharge	
0.25	≥17/≥1000 C[a]	N.A.	
0.50	≥33 /≥1000 C [a]	N.A.	70-vol% PC with water dissolving 0.87-m Zn^{2+} and 3.5-m Na$^+$
0.75	30–35/600–700 C [a]	N.A.	
1.0	20/200–300 C[a]	132/2000 C[d]	
3.0	10/50 C[b]	198/1000 C[e]	50-vol% PC with water dissolving 0.90-m Zn^{2+} and 4.5-m Na$^+$
	59/300 C[c]		

The current densities in charge were estimated from the C rates of synchronous full-charge/discharge in Fig 4c [a], Fig 7a [b], and Fig 7b [c]. The current densities in discharge were estimated based on the charge/discharge mismatch, where the full-charged capacities at low rates of 10 and 300 C were full-discharged at high rates of 2000 and 1000 C in Fig 4b [d] and Fig 7c [e], respectively. In the case of [c], a glass filter was inserted between the cathode and Zn-foil anode to improve the volume of the electrolyte solution. #For improving the cooperative performance between the cathode and anode, it is necessary that the electrolyte conditions are adjusted depending on the loading amounts.

Table S2. Current densities and capacity retention to compare the power and C-rate capacities of previously reported batteries using MHCFs

Active materials (theoretical values (mAh g^{-1}))	Loading amounts of active materials (mg cm^{-2})	*Current densities (mA cm^{-2})	#Capacity retention (%)	References
ZnHCF (66)	0.25	0.165 (10C)	93	This work
		1.65 (100C)	92	
		16.5 (1000C)	90	
	1.0	0.66 (10C)	100	
		6.6 (100C)	100	
		66 (1000C)	100	
		132 (2000 C)	98	
	3.0	198 (1000 C)	100	
ZnHCF (70)	0.5–1	0.050	100	1
		10	89	
		50	67	
ZnHCF (86)	4–5	0.86	80	2
		4.3	74	
		25.8	54	
ZnHCF (110)	1.5–2	0.10	58	3
		0.60	51	
		1.6	32	
NiHCF (60)	2–2.5	0.5	59	4
		25	45	
FeHCF (170)	2.5	0.040	75	5
		2.11	57	
		10.6	40	
MnHCF (125)	~1.5	0.19	89	6
		1.9	56	
		3.8	42	
MnHCF (150)	~1	0.03	91	7
		0.1	74	
		0.5	49	
MnFeNiHCF (150)	1–2	1.5	74	8
		6	71	

*The current densities were calculated based on values of the loading amounts (mg cm^{-2}) and discharge currents (A g^{-1}) as described in the literature. For cases where the discharge currents were not explicitly mentioned, they were assumed based on the C rates and theoretical capacities (mAh g^{-1}). #Similarly, the capacity retention values were based on the theoretical or low-rate capacities.

References

1 Q. Li, K. Ma, C. Hong, Z. Yang, C. Qi, G. Yang and C. Wang, *Energy Storage Mater.,* 2021, **42**, 715–722.

2 M. Huang, J. Meng, Z. Huang, X. Wang and L. Mai, *J. Mater. Chem. A,* 2020, **8**, 6631–6637.

3   F. Ming, Y. Zhu, G. Huang, A.-H. Emwas, H. Liang, Y. Cui and H. N. Alshareef, *J. Am. Chem. Soc.,* 2022, **144**, 7160–7170.

4   Y. Yuan, D. Bin, X. Dong, Y. Wang, C. Wang and Y. Xia, *ACS Sustainable Chem. Eng.,* 2020, **8**, 3655−3663.

5   J. Zhang, J. Zhang, H. Wang, V. W.-h. Lau, G.-H. Lee, K. Zhang, M. Park and Y.-M. Kang, *ACS Energy Lett.,* 2022, **7**, 4472–4482.

6   X. Wu, S. Qiu, Y. Liu, Y. Xu, Z. Jian, J. Yang, X. Ji and J. Liu, *Adv. Mater.,* 2022, **34**, 2106876.

7   L. Deng, J. Qu, X. Niu, J. Liu, J. Zhang, Y. Hong, M. Feng, J. Wang, M. Hu, L. Zeng, Q. Zhang, L. Guo and Y. Zhu, *Nat. Commun.*, 2021, **12**, 2167.

8   Z. Xu, Y. Sun, J. Xie, Y. Nie, X. Xu, J. Tu, C. Shen, Y. Jin, Y. Li, Y. Lu, A. Zhou, F. Chen, T. Zhu and X. Zhao, *Mater. Today Sustainability.,* 2022, **18**, 100113.
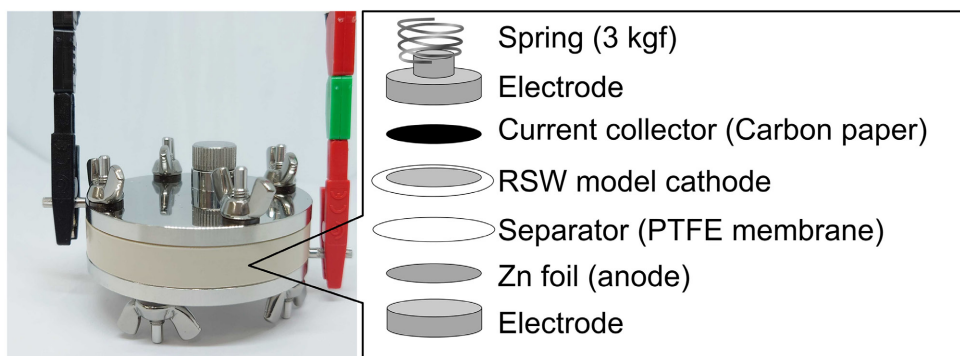
Fig. S1. Cell assembly.
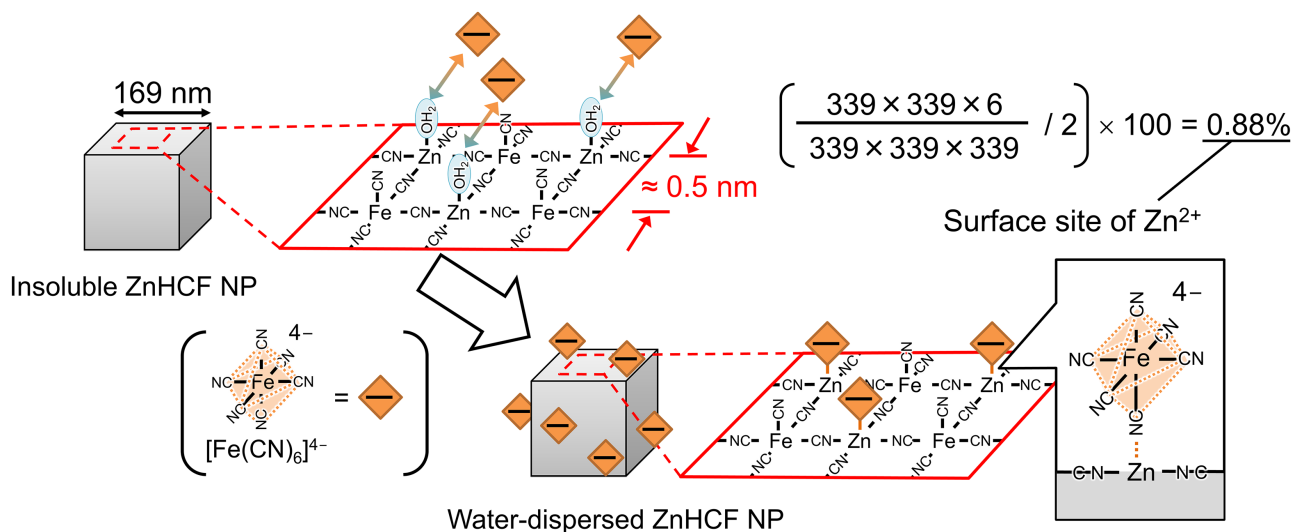
Fig. S2. Calculating a surface-attached amount of $[Fe^{II}(CN)_6]^{4-}$. For an example of an ideal cubic ZnHCF NP, the number of metals (Fe and Zn) is 339, aligned on a 169-nm edge length. H_2O molecules weakly coordinate the surface Zn^{2+} ions before surface modification. When $[Fe^{II}(CN)_6]^{4-}$ binds to the whole surface sites of Zn^{2+} by displacement of the H_2O molecules to form $Zn-[NC-Fe^{II}(CN)_5]^{4-}$, the attached amount of $[Fe^{II}(CN)_6]^{4-}$ is equal to that of the surface Zn^{2+} ($339 \times 339 \times 6 \times 1/2$); therefore, it is calculated as 0.88 mol% versus the total metal amount ($339 \times 339 \times 339$).[48]

11
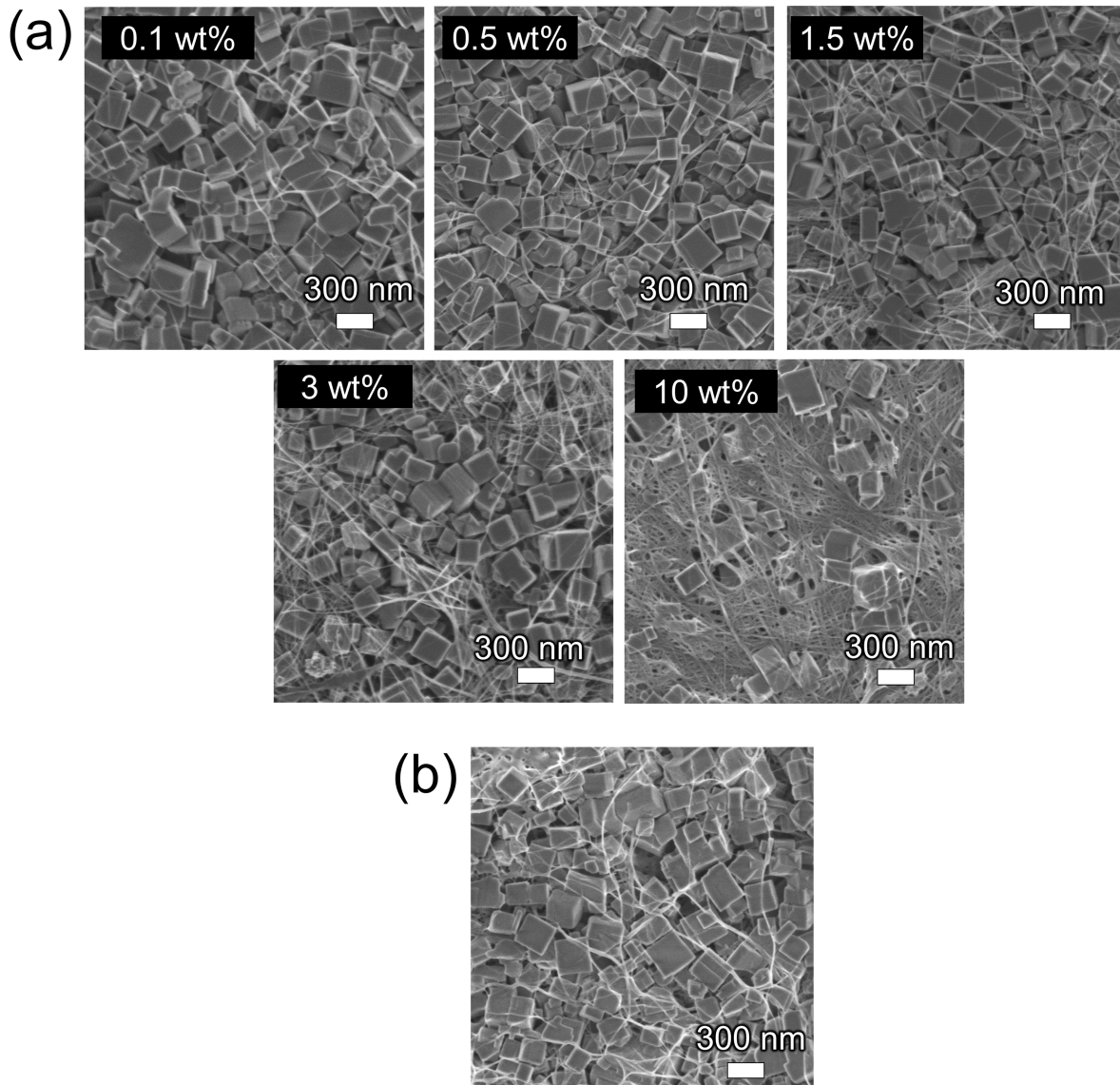
Fig. S3. Top-view FE-SEM images of RSW model cathodes using surface-modified ZnHCF NPs. **(a)** SWNTs between 0.1 and 10 wt%. (b) After the 150,000 cycles of Fig. 4d.
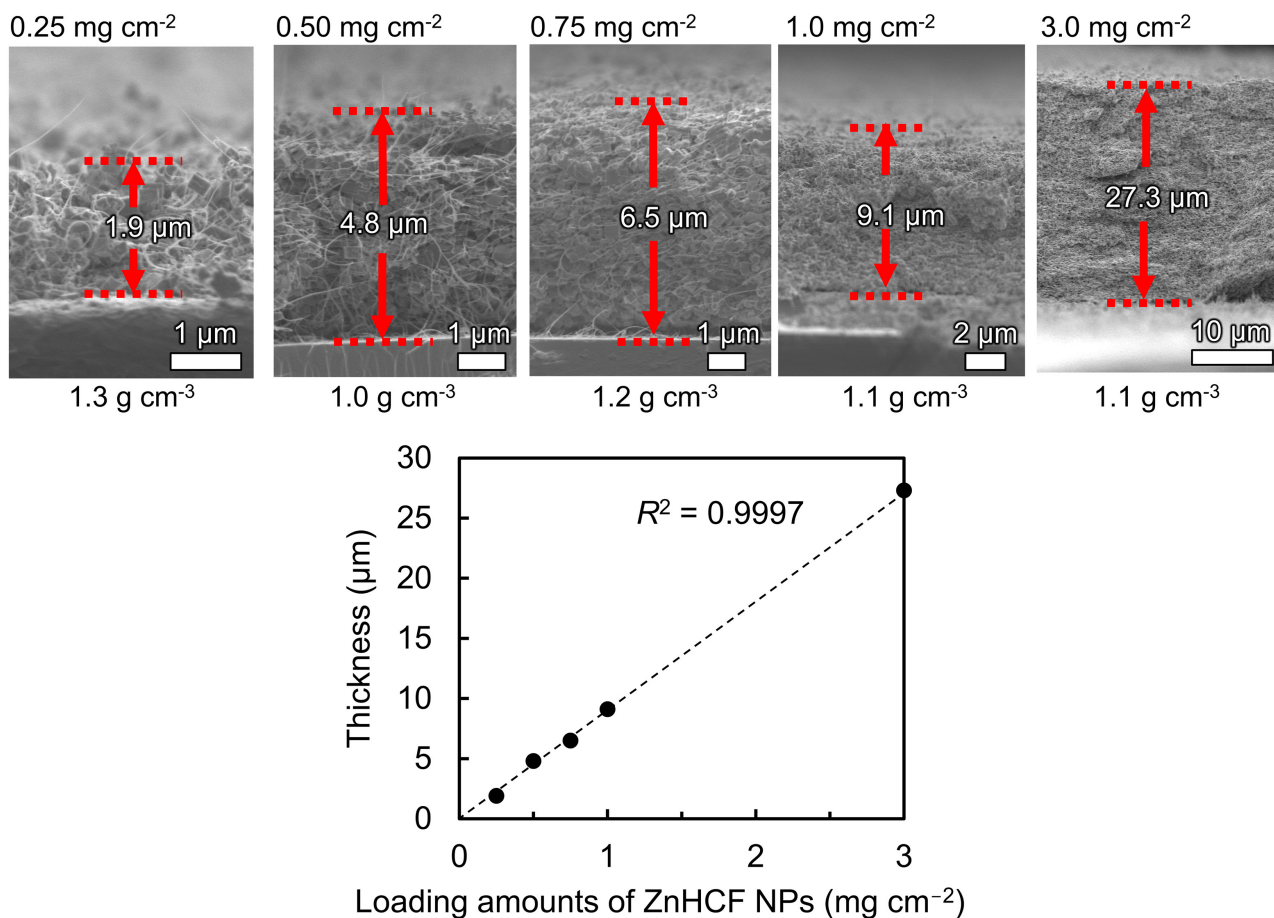
Fig. S4. Cross-sectional FE-SEM images of RSW model cathodes in various loading amounts between 0.25 and 3.0 mg cm^{-2} of surface-modified ZnHCF NPs. The thicknesses are linearly increased by the loading amounts. The bulk densities of surface-modified ZnHCF NPs are ranged between 1.0 and 1.3 g cm^{-3} without large deviation.
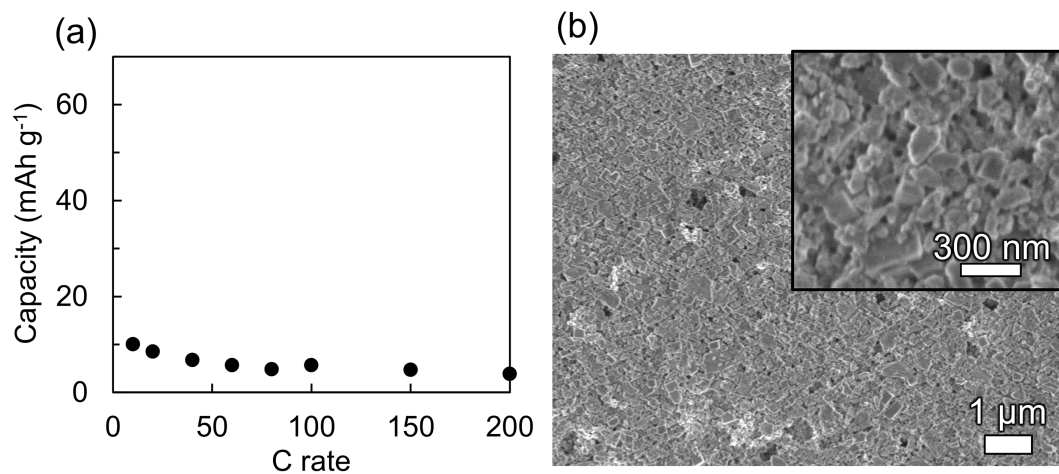
Fig. S5. (a) C-rate capability of a binder-used cathode prepared by long-term mixing surface-modified-free ZnHCF NPs and SWNTs with a binder and solvent and (b) its top-view FE-SEM image. The C-rate capability was measured in 70-vol% PC with water dissolving 0.87-m Zn^{2+} and 3.5-m Na^+.
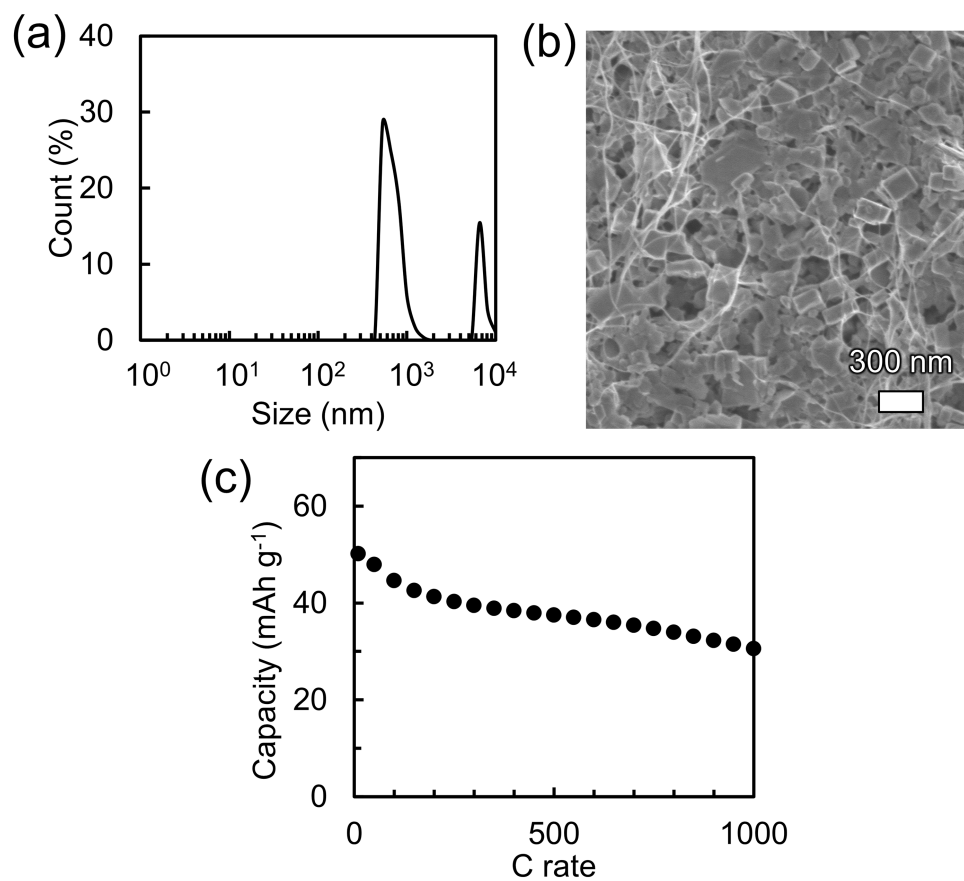
Fig. S6. (a) DLS particle-size distribution of an aqueous suspension of surface-modification-free ZnHCF NPs. (b) Top-view FE-SEM image and (c) capacities depending on C rates of the cathode using the ZnHCF NPs (1.0 mg cm^{-2}) and 1.5-wt% SWNTs.
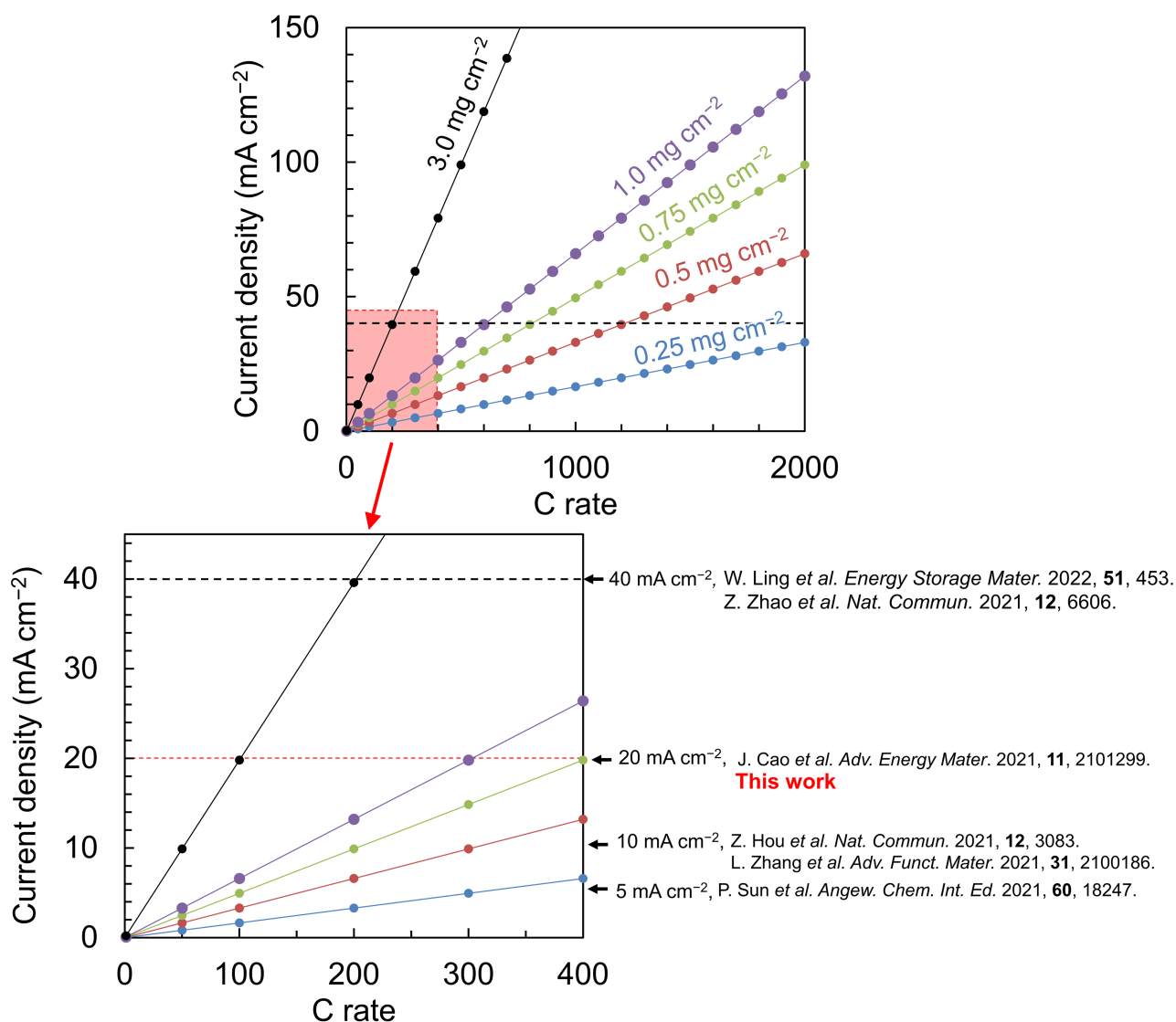
Fig. S7. Relationships between current densities and C rates. The linear relationships of different loading amounts of ZnHCF NPs from 0.25 to 3.0 mg cm^{-2} are expressed based on the maximum current-density value of 20 mA cm^{-2} at 300 C for the synchronous charge/discharge in the standard loading amount of 1.0 mg cm^{-2} (Fig. 4a). The previously reported current-density values of Zn metals are shown by arrows, as summarized in Fig. 3h of ref. 11. Even though the current densities of 20 mA cm^{-2} are maintained, it is difficult in increased loading amounts over 3.0 mg cm^{-2} to fabricate ultrahigh-rate batteries showing >100 C in charging. Nevertheless, in 2022, a single-crystal Zn anode achieved an ultrahigh current density of 200 mA cm^{-2} by ideal dendrite-free epitaxial growth to Zn (002) orientation.[69]
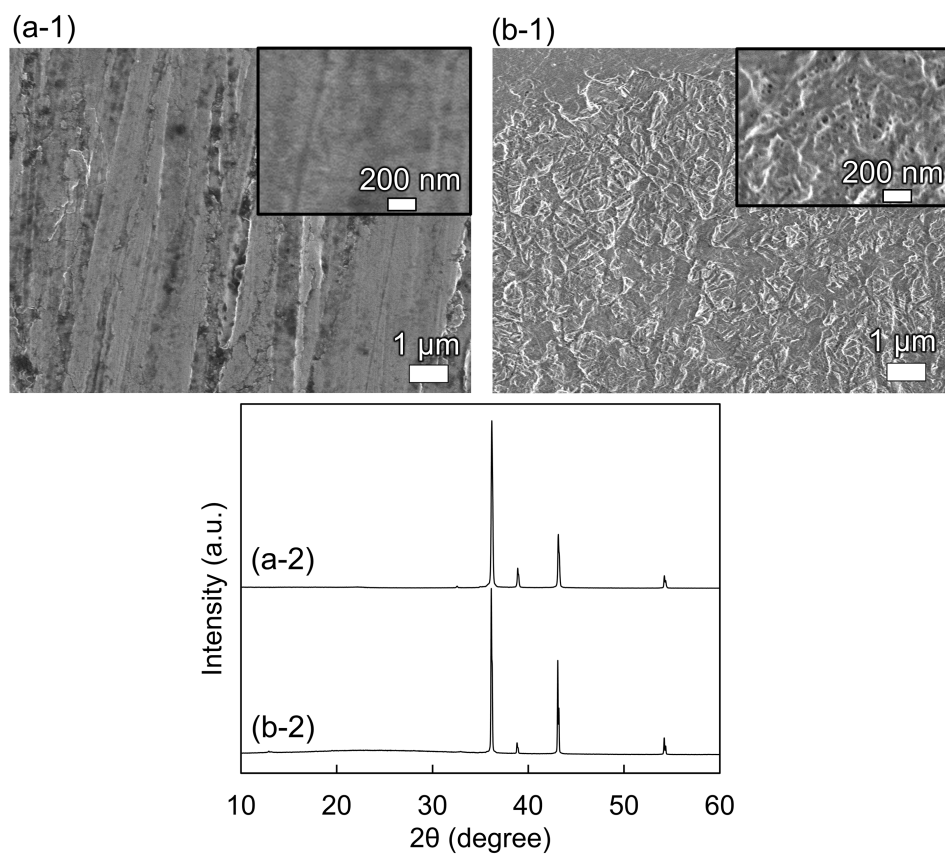
Fig. **S8.** Top-view FE-SEM images and XRD patterns of the pristine Zn-foil anode (a-1 and a-2) and after 150,000 charge/discharge cycles at 400 C (b-1 and b-2).
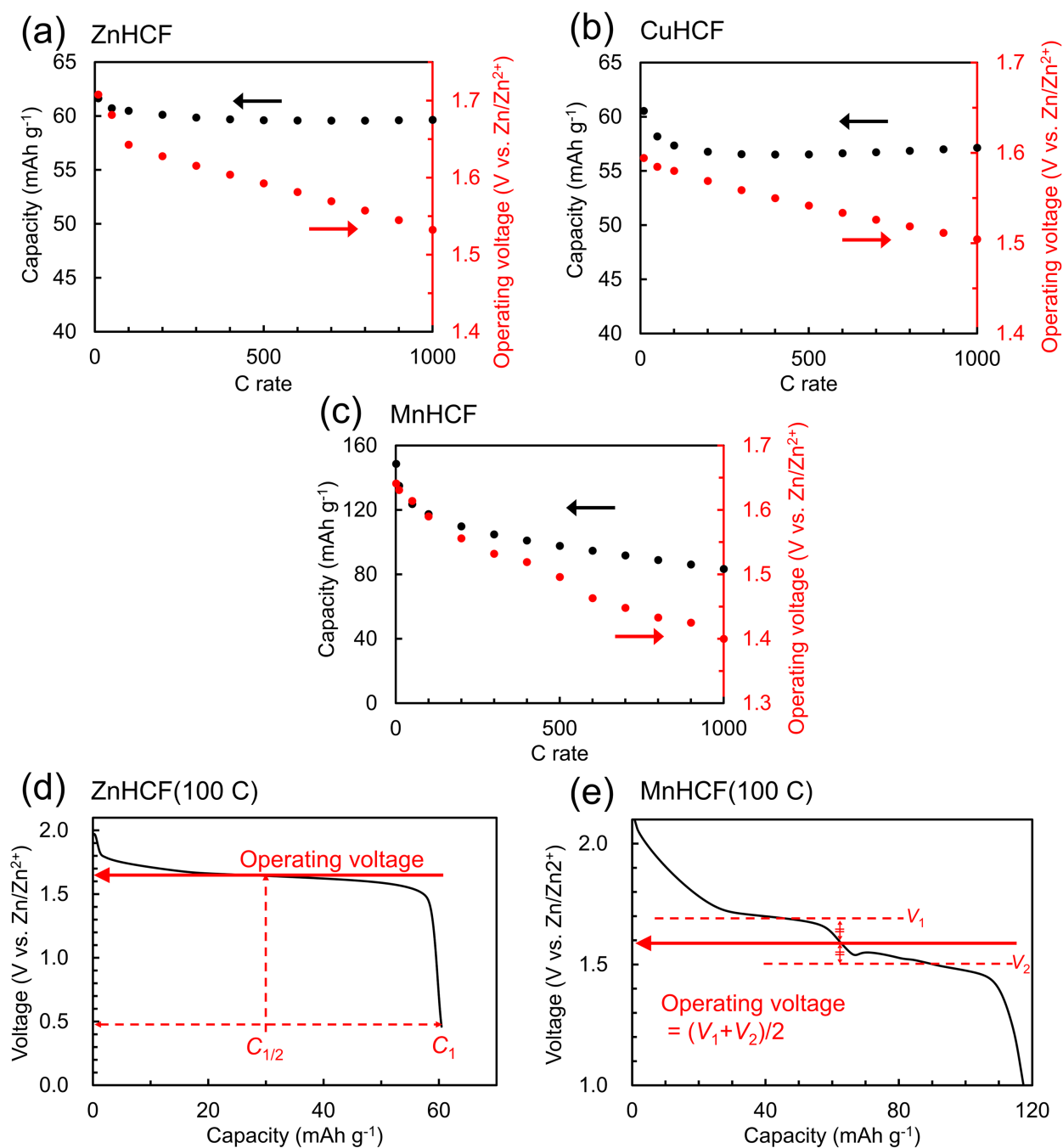
Fig. S9. Operating voltages and capacities depending on C rates of Zn–Na/KIBs using RSW model cathodes to update the Ragone plots (Fig. 6a) based on the charge/discharge profiles of (a) Fig. 4e for ZnHCF, (b) Fig. 5c for CuHCF, (c) Fig. 5f for MnHCF. (d) To determine the energy densities for the Ragone plots (Fig. 6a), the operating voltages of ZnHCF and CuHCF with one-step plateaus are estimated as half-capacity ($C_{1/2}$) voltages. (e) The operating voltages of MnHCF with two-step plateaus are estimated as averaged voltages of half-capacity voltages of V_1 and V_2. When the two-step plateaus are ambiguous, the operating voltages are similarly estimated utilizing the same method as (d).

18
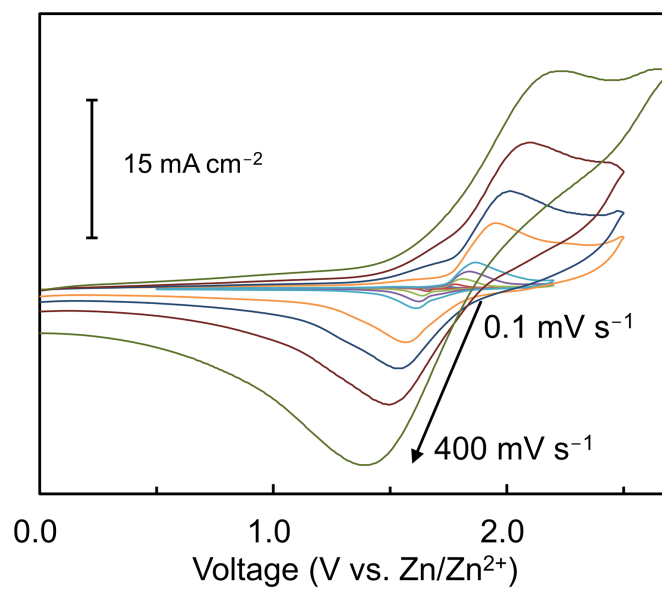
Fig. S10. Cyclic voltammograms of the conventional binder-used cathode (Fig. 3f) in 70-vol% PC with water dissolving 0.87-m Zn^{2+} and 3.5-m Na^+. The loading amount of surface-modified-free ZnHCF NPs is 0.25 mg cm^{-2}.

Surface-modified MnHCF NPs　　RSW model cathode
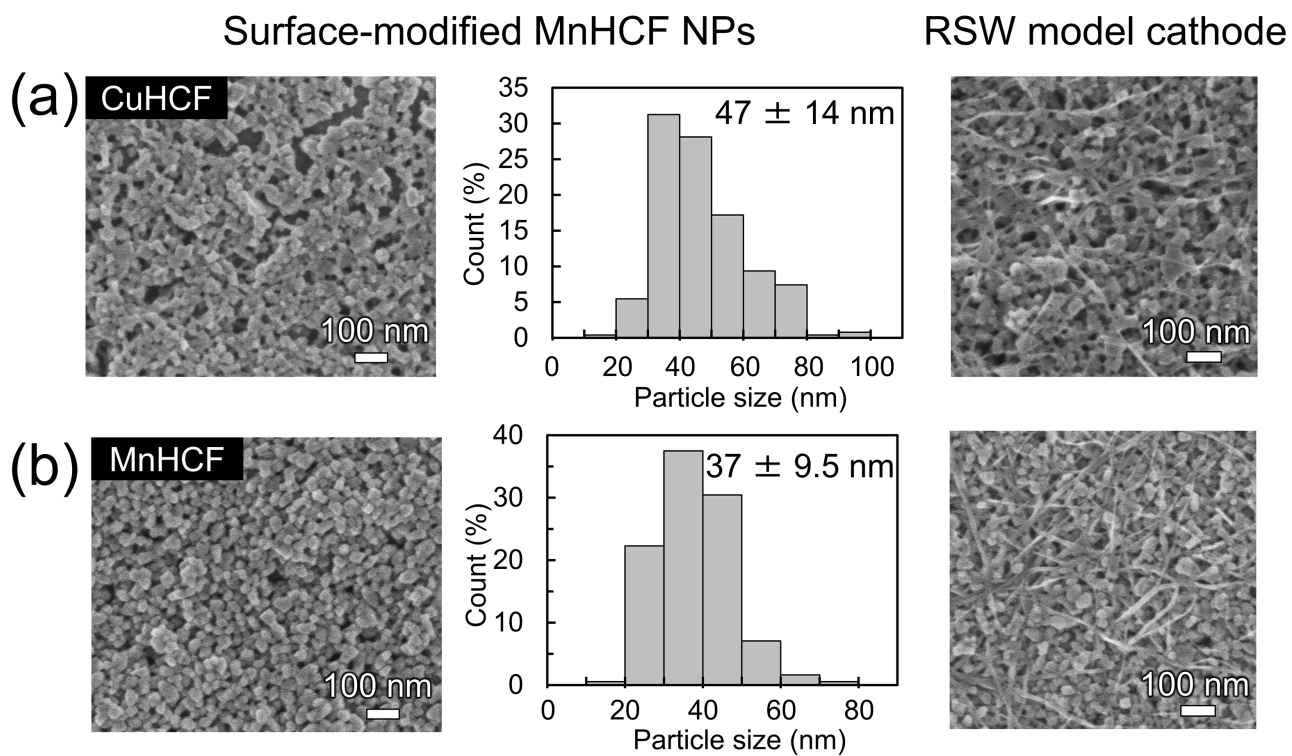
Fig. S11. FE-SEM images of surface-modified MHCF NPs and particle-size histograms and top-view FE-SEM images of RSW model cathodes with surface-modified MHCF NPs of CuHCF (a) and MnHCF (b). In the RSW model cathodes, the loading amount of MnHCF NPs is 0.50 mg cm^{-2} and SWNTs are 3 wt%.
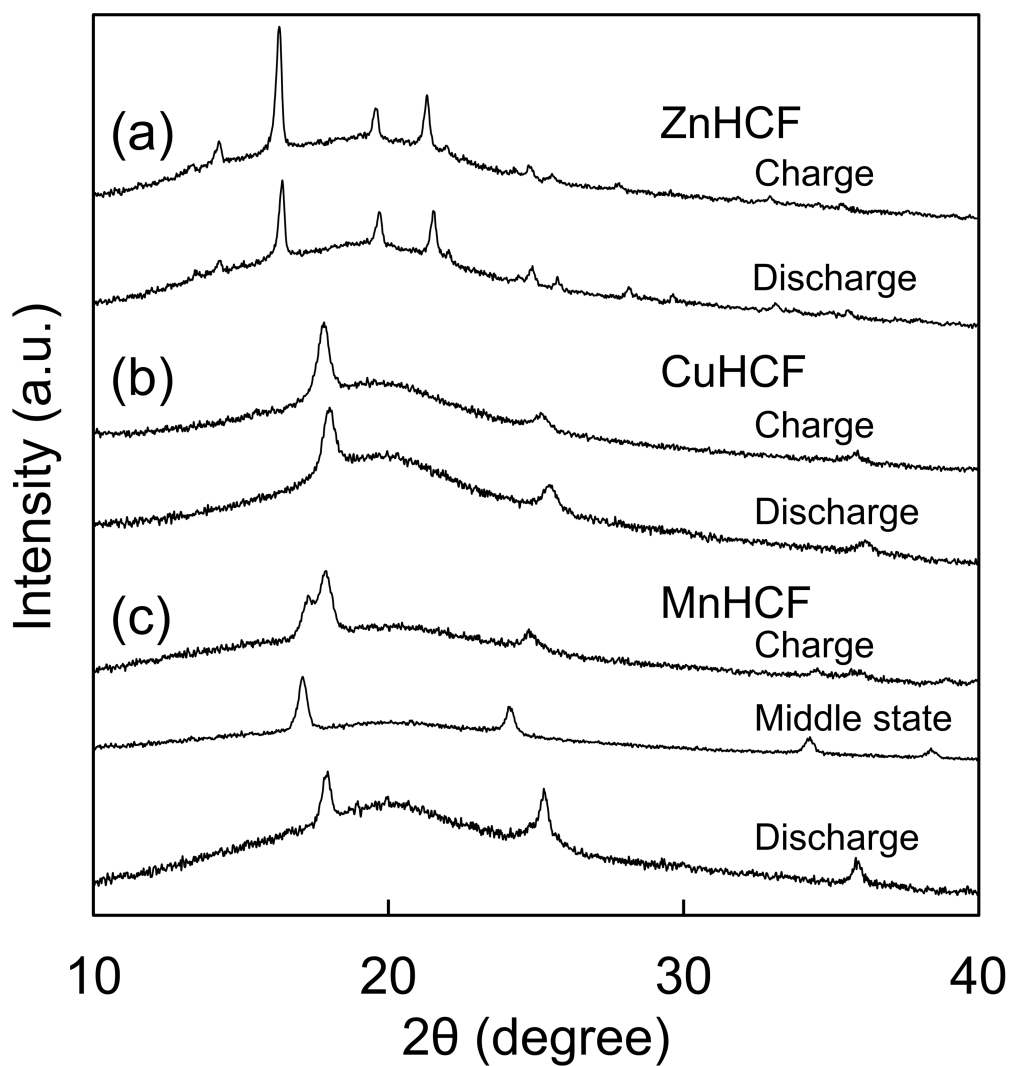
Fig. S12. Changes in XRD patterns during the charge/discharge processes of Zn–Na/KIBs using RSW model cathodes with surface-modified MHCF NPs of (a) ZnHCF, (b) CuHCF, and (c) MnHCF. In the cases of MnHCFs (c), the XRD pattern of the middle state was measured at mid-voltages of the two-step plateaus based on Fig. 5e,f.